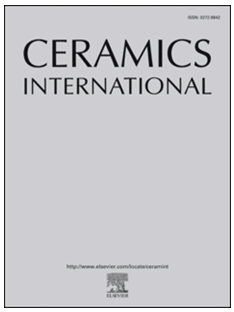

Evaluating the Dynamic Integrity of Ruthenium Oxide Nanoparticles using Shock Tube: An Integrated Experimental and DFT Study

Surendhar Sakthivel, Sivaprakash Paramasivam, Martin Britto Dhas Sathyadhas Amalapushpam, Aravindan Vivekanandan, Jithesh Ramakrishnan Kannan, Tobias Hermann, Ikhyun Kim

PII: S0272-8842(26)00657-7

DOI: https://doi.org/10.1016/j.ceramint.2026.02.116

Reference: CERI 51094

To appear in: *Ceramics International*

Received Date: 18 November 2025

Revised Date: 29 January 2026

Accepted Date: 8 February 2026

Please cite this article as: S. Sakthivel, S. Paramasivam, M.B. Dhas Sathyadhas Amalapushpam, A. Vivekanandan, J.R. Kannan, T. Hermann, I. Kim, Evaluating the Dynamic Integrity of Ruthenium Oxide Nanoparticles using Shock Tube: An Integrated Experimental and DFT Study, *Ceramics International*, https://doi.org/10.1016/j.ceramint.2026.02.116.

Evaluating the Dynamic Integrity of Ruthenium Oxide Nanoparticles using Shock Tube: An Integrated Experimental and DFT Study

Surendhar Sakthivel[a], Sivaprakash Paramasivam[a], Martin Britto Dhas Sathyadhas Amalapushpam[a], Aravindan Vivekanandan[b], Jithesh Ramakrishnan Kannan[b], Tobias Hermann[c], Ikhyun Kim[a,*]

[a]*Department of Mechanical and Engineering, Keimyung University, Daegu 42601, Republic of Korea*

[b]*Smart Materials Research Laboratory, Department of Physics, Thiagarajar College of Engineering, Madurai 625015, Tamil Nadu, India*

[c]*Department of Engineering Science, University of Oxford, Southwell Building, Osney Mead, Oxford, OX2 0ES, Oxfordshire, United Kingdom*

Corresponding author: kimih@kmu.ac.kr

Abstract

In the present work, the structural, morphological, molecular, optical, and catalytic features of RuO_2 were evaluated for their stability using a tabletop shock tube and compared with results from density functional theory (DFT) calculations. Based on the XRD patterns that were obtained, it was discovered that the average crystalline sizes for the control, 200, and 400 shocked RuO_2 nanoparticles were 22.8, 23.7, and 23.6 nm, respectively. RuO_2 remained morphologically stable after 400 shocks, and the calculated average grain sizes were 26.98, 24.52, and 25.66 nm. The molecular stability of the nanoparticles was assessed by FTIR, and the results suggest there were no major changes in the RuO_2 NPs. XPS analysis confirmed the chemical stability of RuO_2 under dynamic shock conditions, with Ru maintaining its predominant Ru^{4+} oxidation state and showing negligible variation in the oxygen environment. Methylene Blue dye was used with the control and shock-treated RuO_2 NPs as a catalyst to evaluate the photo-assisted degradation activity under sunlight exposure. The RuO_2 NPs exhibited excellent stability under these extreme conditions.

Keywords: RuO_2, Shock wave, stability, Photocatalyst, DOS

1. Introduction

The acoustic shock wave-induced approach is one of the simplest and cost-effective approaches that can be utilised to tune the properties of a material [1]. When compared to other methods, such as electron, proton, and gamma irradiation settings, high-pressure tests are the least complicated approach for determining which materials are acceptable for use in space and extreme environments [2,3]. These applications have fundamental needs that depend on the performance of the materials with traits of high durability, sensitivity, and mechanical stability against the effects of extreme conditions [4]. Research of this nature, which pertains to applications that involve high temperatures, such as thermal manufacturing devices and components for space shuttles, is becoming increasingly necessary [5]. Especially, the shock wave recovery experiments on NPs provide a deeper understanding of material stability. Additionally, nanomaterials have the potential to experience phase transition, recrystallisation, amorphisation, and distortion as a result of structural changes that take place during shock wave loading. These transformations can take place under circumstances of high dynamic pressure and temperature [6] [7] [8]. Particularly, the remarkable uses of metal oxide nanoparticles (NPs) have prompted researchers to seek stable materials that can withstand extreme conditions. Several notable shock wave recovery experiments on metal oxides have been reported, including the anatase-to-rutile phase transformation in TiO_2 [5], the examination of structural and morphological stability in $SrTiO_3$ [6], and stability studies of ZnO [9] and AgO [10]. Although many metal oxides have been investigated so far, no shock wave recovery investigations have been reported on RuO_2. RuO_2 crystallises in a Rutile structure, which is also the prevalent form of TiO_2 [11]. RuO_2 is a semiconductor with relatively high electrical conductivity, making it useful in a variety of applications, including catalysis [12] [13] and electronics [14]. Particularly, RuO_2 greatly increases

photocatalytic performance in mesoporous heterostructures as a co-catalyst alongside TiO_2 by promoting charge separation and inhibiting electron–hole recombination. For example, Uddin et al. reported that RuO_2/TiO_2 mesoporous composites, when irradiated with UV–visible light, produced hydrogen and degraded organic pollutants at significant rates [15]. Similarly, it was shown that RuO_2/TiO_2 nanobelt heterostructures degraded benzyl alcohol more effectively than P25 TiO_2, which was attributed to the improved band alignment and faster interfacial charge transfer [16]. RuO_2 is an attractive material for photocatalytic applications due to its high surface activity, favourable rutile-phase band structure, and excellent conductivity [17]. However, when shock wave processing is considered, where high temperatures and pressures cause quick structural and electronic changes, it is essential to evaluate how these powerful stimuli impact the photocatalytic performance of RuO_2. Charge carrier mobility, surface active sites, and heterojunction integrity with TiO_2 could be altered by shock-induced phase changes and defect formation [18]. Therefore, comparing the photocatalytic performance of RuO_2 before and after shock-loading standardised dye degradation assays will reveal how shock impacts its catalytic turnover, surface area, and electron–hole separation efficiency. This method situates the study of nanoparticle stability under shock waves in both fundamental and application-driven contexts by directly linking RuO_2's structural-electronic robustness to its known photocatalytic efficiency.

Although RuO_2 catalytic reactions have been extensively investigated, virtually nothing is known about how it performs under shock wave conditions, which is a critical concern for aerospace and military industries. Examining RuO_2's behaviour under shock wave conditions enables us to determine its resilience, longevity, and functionality in extreme conditions. This information is critical for understanding the robustness of RuO_2 electrocatalysts in aerospace and military systems' propulsion, energy conversion, and sensing applications,

which are exposed to extremely harsh environments. To optimise a catalyst that can withstand harsh working conditions, it is important to grasp how shock waves affect RuO_2. The current shock recovery study aims to investigate the structural, morphological, optical, and electrochemical resilience of RuO_2 nanoparticles NPs by subjecting them to the impulsion of supersonic shock waves. Remarkably, to the best of our knowledge, no studies have reported on RuO_2 NPs when subjected to dynamic shock wave flow exposure.

2. Materials and methods

2.1. Synthesis of RuO_2 by the sol-gel method

A modified sol-gel approach was used to synthesise the RuO_2 NPs (refer to Fig.1). The metal precursor in a standard process was ($RuCl_3 \cdot xH_2O$) ruthenium (III) chloride hydrate. A clear, uniform solution was produced by dissolving an appropriate amount of $RuCl_3$ in deionised water while stirring constantly. A few drops of citric acid were added to start the gelation process, which acts as a chelating agent. Then, ammonia solution (NH_4OH) was slowly added to adjust the pH to around 7. To make sure the mixture was completely complexed and gelled, it was swirled constantly at room temperature for a few hours. A dark-coloured xerogel was produced by ageing the resultant sol for 12 hours and then drying it in a hot air oven at 80°C. To facilitate the crystallisation of RuO_2 and eliminate any organic residues, the dried gel was subsequently subjected to three hours of air-fired calcination in a muffle furnace set at 500°C. For subsequent characterisation, the finished product was fine-ground into a powder and preserved in an airtight container.

Figure 1: Schematic representation for Sol-gel synthesis of RuO_2 NPs.

2.2. Photocatalyst details

As a model organic pollutant, we used methylene blue (MB) in an experiment that involved the degradation of the dye [19]. The purpose of this experiment was to determine how the photo-assisted degradation activity of RuO_2 nanoparticles changed before and after the shock wave treatment. A standard procedure involved combining 10 mg of RuO_2 nanopowder with 100 ml of an MB solution in water at a concentration of 10 mg per litre. To bring the dye molecules and the catalyst surface to a state of equilibrium between adsorption and desorption, we stirred the solution continuously with a magnet in the dark for a period of thirty minutes [20].

2.3. Analytical Characterisation Details

X-ray diffraction (XRD) was performed using a Rigaku Smart Lab XRD made in Japan. The X-ray source utilised was CuKα1 with a wavelength of

1.5407 A˚. Using the assistance of a TESCAN VEGA3 SBH scanning electron microscope (SEM), the morphological properties of the specimens were investigated. A 532 nm laser excitation source was used to conduct the Raman analysis using a Renishaw inVia Raman Microscope. The range of 100-1000 cm^{-1} was used for spectral collection, and the spectral resolution was around 1 cm^{-1}. X-ray photoelectron spectroscopy (XPS) was used with a monochromatic Al Kα source in a K-Alpha+ XPS system manufactured by Thermo Scientific. An integrating sphere attachment was used to analyse the optical properties with a Shimadzu UV-2600 spectrophotometer in diffuse reflectance mode. The spectra were captured within the 200-800 nm wavelength range.

2.4. Shock wave loading

In this investigation, the RuO_2 samples were split into three sections; one sample was preserved as a control, and the other two were subjected to 200 and 400 shock pulses, respectively, to load the shock waves. The shock waves were produced using a semi-automatic Reddy Tube (shown in Fig. 2)[21,22]. The samples that were tested were positioned in the sample holder, which was typically positioned 1 cm away from the open end of the shock tube on average. After that, shock pulses with a 5-second interval between each shock pulse were loaded onto the test samples. The shock pulses repeatedly strike the test sample with 200 and 400 shock pulses, maintaining a two-second interval between consecutive pulses. It is worth noting that the duration of each pulse (test time) is 2.5 milliseconds. There was a transient pressure of 0.59 MPa and a temperature of 520 K during a single shock pulse [23]. The detailed shock wave loading procedure has already been published in [24]. The dynamic loading conditions are roughly equivalent to sustained atmospheric flight at sea level with a Mach number of approximately 4.1 or a velocity of 1400 m/s. Utilising chemical equilibrium calculations across a normal shock wave at these conditions confirms that the dynamic loading case reaches 74% of the post-shock temperature of the

flight case. Future experiments required to verify material response to high-speed flow conditions would require testing in a continuous high-temperature flow [25].

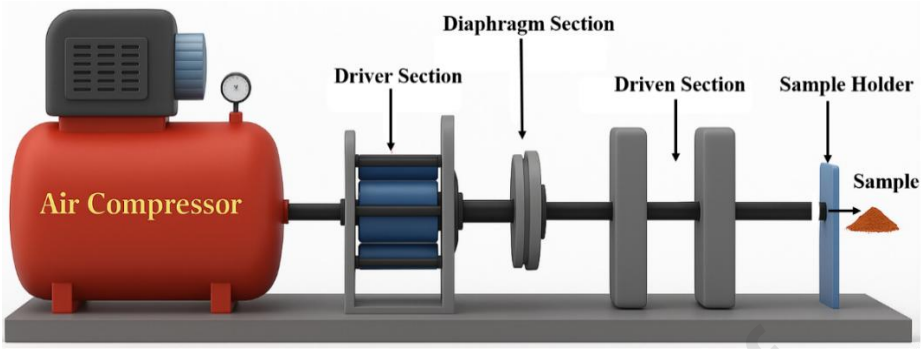

Figure 2: Schematic illustration of the tabletop shock tube used in the current investigation.

2.5 Theoretical calculations

We carried out structural, optical, and electronic analyses of RuO_2 in the rutile structure using density functional theory (DFT) within the framework of the Full Potential and Linearized Augmented Plane Wave (FP-LAPW) method [26–28]. The exchange–correlation functional within the Generalised Gradient Approximation (GGA), as parameterised by the Perdew–Burke–Ernzerhof (PBE) scheme, was used in this calculation. The muffin-tin radii (RMT) were set to 1.95 a.u. for Ru and 1.68 a.u. for O to prevent charge leakage from the muffin-tin spheres. For the self-consistent field calculations, a Monkhorst–Pack grid consisting of 3000 k-points was used to ensure accurate Brillouin zone sampling. The angular momentum cutoff was set to lmax = 12, while the plane-wave cutoff parameter was chosen as RMT × Kmax = 7. The convergence thresholds were fixed at 10^{-5} Ry for the total energy and 10^{-5} e for the charge density, respectively.

3. Results and discussion

3.1. Structural stability analysis (Experimental)

An X-ray diffractometer was used to examine the structural stability of RuO_2 NPs and the degree of crystallinity of these particles when they are

subjected to shock wave loading. Fig. 3(a) shows the diffraction profiles of the control and shocked RuO_2 NPs that were obtained from the analysis of their structural properties. Understanding the crystal structure of RuO_2 NPs under control conditions is necessary before delving into the impact of shock waves. The mere fact that the diffraction peaks are so sharp serves as proof that the RuO_2 possesses a good crystalline nature. The XRD pattern obtained suggests that the RuO_2 NPs have a tetragonal structure with *P4_2/mnm* space group, which is consistent with the reported literature (Fig. 4(d)) [29]. It was observed that there were considerable changes taking place in the intensities of the crystalline plane when the samples were loaded with 200 and 400 shock pulses, as shown in Fig. 3(b& c). However, a modest shift of the diffraction planes towards the higher-angle side was detected for 200 and 400 shock-loaded samples. This indicates that the presence of the minimal shock does not have an effect on the crystal structure of RuO_2. The mild peak shift is caused by the shock-induced structural defect [30]. Fig. 3(c) indicates that the XRD pattern slightly shifts to a higher angle under shocked conditions due to the transient temperature and pressure. Generally, when materials are subjected to supersonic shock pulses, they are compressed, which productively influences lattice relaxation and strain, leading to the shortening of bonds and inducing changes in atomic positions and the lattice. Interestingly, when the shock pulses leave the lattice, it undergoes sudden expansion, leading to atomic oscillations, and once the atoms reach their equilibrium positions, they retain either their original or newly formed positions. In our case, we observed a minor shift towards a higher angle from control to 400 shocks attributed to the lattice contraction, due to residual strain, lattice defects, or rearranged atomic positions, leading to a measurable shift in the XRD. At 400 shock pulses, no phase transformation has been observed, and no new peaks have appeared, and existing peaks have disappeared.

Further, the crystalline size of the samples was calculated using the Scherrer equation shown in Table 1. The calculated structural parameters indicate that the shocked NPs are structurally stable with only slight fluctuations in the parameters. To further validate the results, Rietveld refinement analysis was performed for the control and shock-treated samples. Fig. 4(a-c) shows the Rietveld refined XRD patterns, and the calculated unit cell parameters are presented in Table 1. The refined unit cell parameters are shown in Table 2. The results suggest that the shock-treated RuO_2 sample is structurally stable without any changes in unit cell volume.

3.2 Calculated Structural properties of RuO_2

The RuO_2 crystallises in the tetragonal phase with the space group $P4_2/mnm$ (No. 136). The stable crystal structure of RuO_2 in the rutile-type arrangement is illustrated in Fig. 4(d). To obtain the equilibrium structural properties, we performed a volume optimisation of the stable phase. The resulting energy–volume data were fitted using the Birch–Murnaghan equation of state, from which the ground-state properties were derived. These include the optimised lattice parameters (Å), equilibrium volume (a.u.^{3}), and ground-state energy (Ry), as summarised in Table 3. The fact that the findings of the experiments and the theoretical calculations are so closely aligned substantiates the dependability of the model and verifies the XRD characteristics that were observed as being intrinsic to the material

.

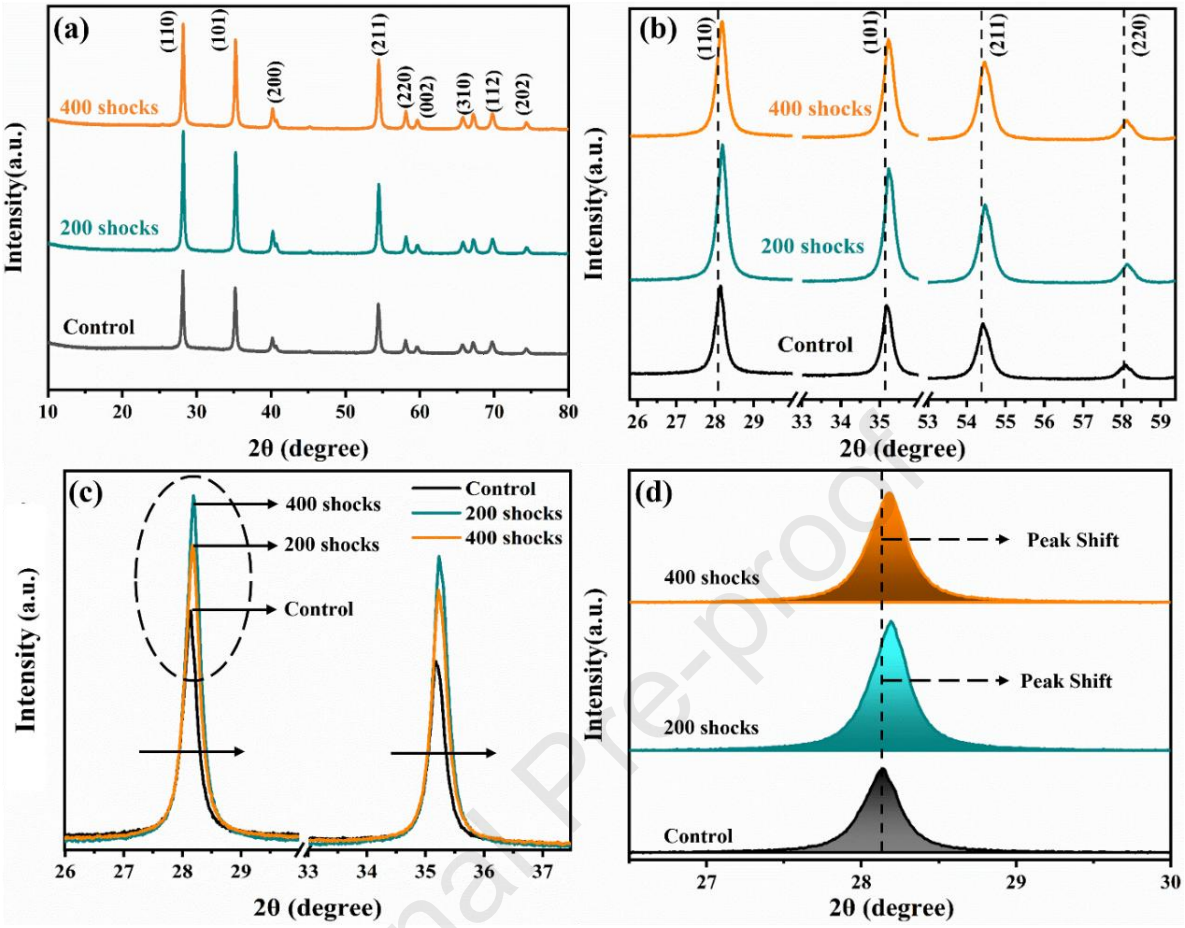

Figure 3: XRD patterns of the **(a&b)** control and shocked RuO_2, **(c)** peak shift in the shocked RuO_2, **(d)** crystal structure of the RuO_2.

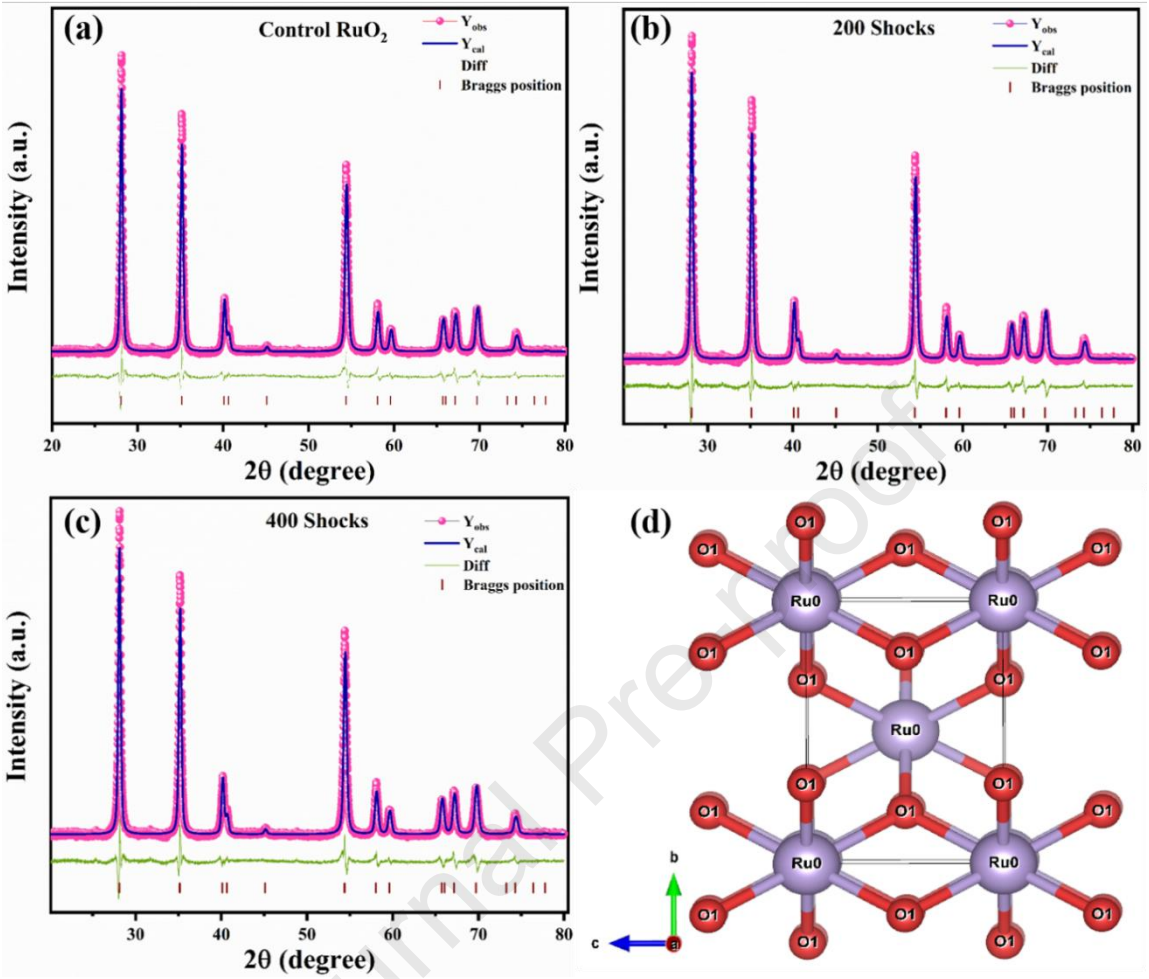

Figure 4: Reitveld refinement plots for **(a)** control, **(b)** 200 shocked, **(c)** 400 shocked RuO_2, **(d)** crystal structure of the RuO_2.

Table 1: Structural parameters of the control and shocked RuO_2

Condition	Crystalline size (nm)	Dislocation density	Micro strain
Control	22.84	1.788	6.02
200 shocks	23.07	1.877	6.16
400 shocks	23.64	1.916	6.25

Table 2: Reitveld Refinement Parameters

Parameters	**Control**	**200 shocks**	**400 shocks**
a(Å)	4.490	4.487	4.486
c(Å)	3.100	3.091	3.095
V(Å^3)	62.503	62.341	62.340
Structure	Tetragonal	Tetragonal	Tetragonal
Space group	*$P4_2$-mnm*	*$P4_2$-mnm*	*$P4_2$-mnm*
R_{WP}	9.1	9.2	9.1
GOF	2.1	2.2	2.1

Table 3. The optimised ground-state properties of the RuO_2 using DFT calculations through theoretical predictions

Study	**Lattice Parameters**		**Equilibrium Volume (a.u^3)**	**Ground-state Energy (Ry)**
	a = b (Å)	**c (Å)**		
Control	4.482	3.111	62.508	-18729.341
200 shocks	4.472	3.118	62.501	-18729.2840
400 shocks	4.486	3.097	62.500	-18729.2837

3.3 SEM analysis

Scanning electron microscopy (SEM) was performed to analyse any changes in the morphological properties that may have occurred as a result of the shock wave impulsion in the RuO_2 NPs. Fig. 5 shows the SEM images of the control and shocked RuO_2 NPs. Fig. 5(a-c) demonstrates that the morphology of the shocked RuO_2 NPs remains consistent over a period of 400 shocks. When they were subjected to 200 shock pulses, the size of the particles was greatly reduced. Fig. 6(a-c) shows the calculated average grain size for the shocked and

control RuO_2 NPs. It shows that the average grain size is 26.98, 24.52, and 25.66 nm for the control, 200, and 400 shock-treated RuO_2 NPs. Furthermore, after the implosion of shock waves, the grain size remained stable without any major alterations. Moreover, as seen in the XRD analysis, the stability of the structure was preserved under shock-wave loading; however, minor morphological changes were observed as a result of the impacts of the shock waves, similar to those reported under high-energy irradiation. Morphological analysis revealed that the average grain size was slightly smaller in the sample subjected to 400 shock waves compared to that subjected to 200 shocks. Surface area to volume ratios tend to be higher for materials with smaller grain sizes. With more room to spread out, catalytic reactions like the oxygen reduction reaction can take place.

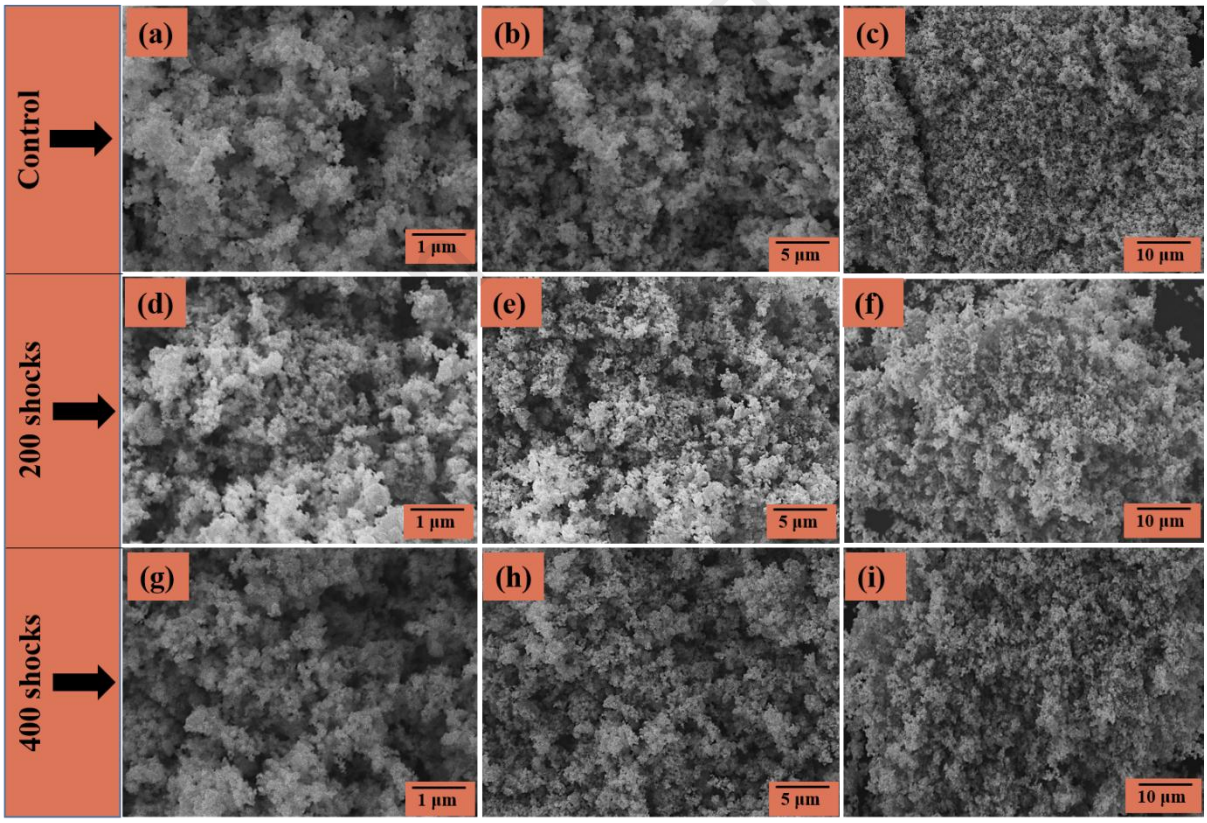

Figure 5: Various resolutions of SEM images for **(a-c)** control, **(d-f)** 200 shocked, and **(g-i)** 400 shocked RuO_2.

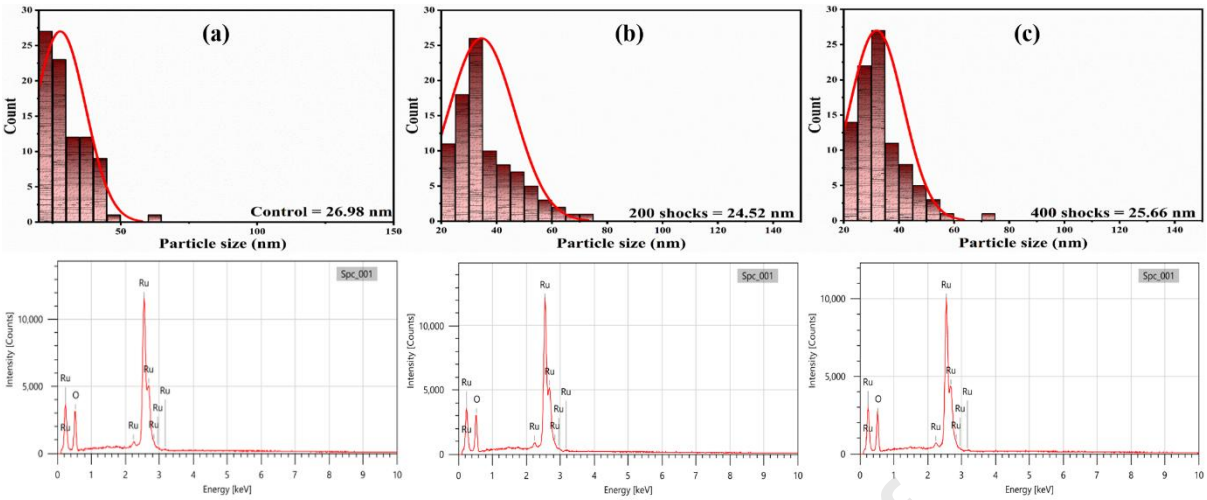

Figure 6: Calculated average particle size and EDX for **(a)** control, **(b)** 200 shocked, **(c)** 300 shocked RuO_2.

3.4 Molecular stability analysis

Fourier transform infrared spectroscopy (FTIR) was used on shock-wave-treated NPs to examine modifications in surface functional groups and molecular structures induced by the shock waves. The vibrational bands of both the control and shocked RuO_2 NPs were recorded at room temperature, with the wave number ranging from 400 to 4000 cm-1. Fig. 7 presents the infrared spectra of the control, 200, and 400 shocked samples. The resultant IR band waves for both the control and shocked samples are exceptionally reminiscent of values found in published work [16].

A distinctive vibrational mode of rutile RuO_2 was detected at 756 cm^{-1} in both the control and shock-treated RuO_2 NPs [31]. A defining feature of peroxo groups is the absorption band observed at ~1019 cm^{-1}. The bands at ~1404 and ~1678 cm^{-1} are attributed to the bending vibrations of water molecules [32]. An absorption peak at ~3089 cm^{-1} corresponds to the stretching vibration of –OH groups. Fig. 7 shows that under the 400 shock-loaded condition, the OH stretching intensity increased. The observed increase in –OH stretching intensity

in the FTIR spectra following shock-wave loading may be attributed to an increase in the concentration of surface hydroxyl groups. It is noteworthy to consider that the outcomes suggest that the peaks of the RuO_2 NPs were the same both before and after the shock loading, despite a slight increase in intensity. Regardless of the high shock wave pressure that was applied, there were no major changes in the location or composition of the RuO_2 NPs. This result substantiates the assertion that the molecular structure of the nanoparticles remained stable following 400 shock pulses.

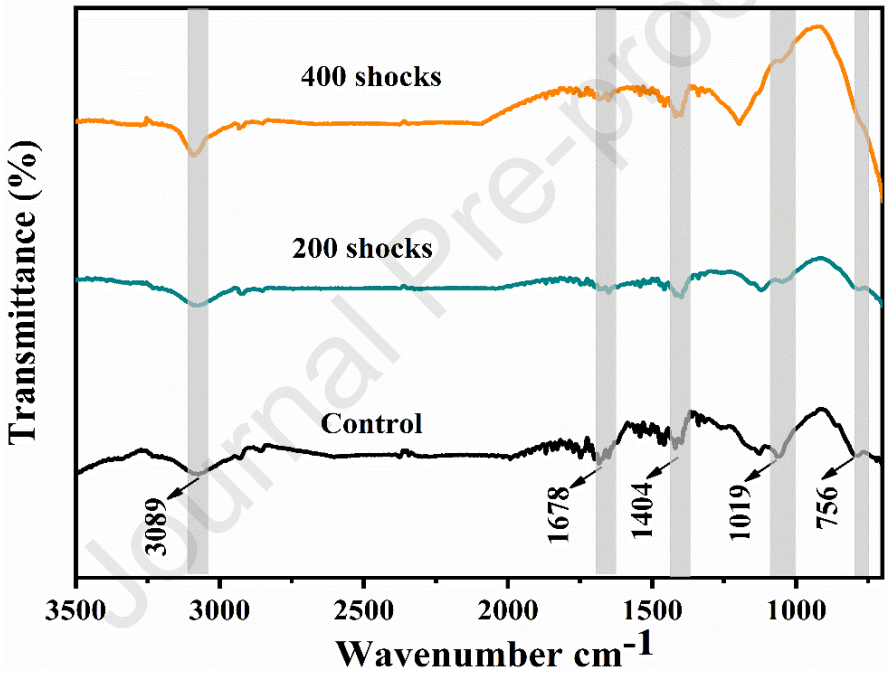

Figure 7: FTIR spectra of the control, 200, and 400 shocked RuO_2.

3.5 Raman analysis

Raman spectroscopy was used to evaluate the structural integrity and vibrational features of the RuO_2 nanoparticles before and after dynamic shock wave treatment. All of the samples, including the control, the 200-shock, and the 400-shock treated samples, exhibited significant and well-defined peaks that corresponded to the typical vibrational modes of rutile-structured RuO_2, which

can be seen in Fig. 8. The primary Raman active modes were observed at 520 cm^{-1} (E_9), ~635 cm^{-1} (A_{1g}), and ~710 cm^{-1} (B_{2g}) [33]. This observation is in line with the reported literature on rutile RuO_2. It is important to note that there was virtually no peak shifting or broadening detected throughout the samples that were subjected to the shock treatment. This result suggests that the crystallographic phase and local bonding environment of RuO_2 remain unchanged even when subjected to mechanical loading of up to 400 shocks. After the shock process, the sharpness and symmetry of the peaks further confirm that the long-range order was maintained and that minimal defects were introduced. A discernible rise in the intensity of the Raman peaks has been found to occur in conjunction with the increase in the number of shock pulses. To be more specific, the vibrational modes E_g, A_g, and B_{2g} demonstrate a notable increase in intensity when subjected to shocked conditions. This behaviour provides evidence that shock wave treatment contributes to the modification of the local structural ordering and the enhancement of the lattice vibrations that are associated with these modes. Fig. 9(a-c) illustrates the quantitative change in peak intensities that correspond to various planes and shock numbers. This demonstrates that there is a systematic association between the intensity of the shock and the activity of the phonons. Because the applied pressure mitigates small structural distortions and amplifies phonon activity, a phenomenon known as shock-induced lattice ordering accounts for the subtle intensity enhancement. The shock waves give the molecules the energy they need to break through local energy barriers, which lets them move from a kinetically confined, deformed state (the control) to a more thermodynamically stable, highly crystalline state. This "healing" of lattice defects that were already present makes the scattering centres line up more evenly, which makes the Raman scattering more efficient and the peak intensity higher. This behaviour aligns with recent research by Sivakumar et al., which demonstrated that d-tartaric acid crystals exposed to shock waves transitioned from a deformed state to a highly crystalline state, indicated by an increase in the

intensity of internal Raman modes rather than a decrease[34–36]. That the material's structural stability has been maintained even when subjected to dynamic shock waves is confirmed by this.

The consistency of the Raman spectra across a range of shock pulses suggests that RuO_2 maintains exceptional mechanical and vibrational stability even under extreme dynamic conditions. The ability to withstand shock or impact is essential for applications in hostile environments, such as those encountered in aerospace and defence systems. Additionally, the stable phonon modes suggest that the electrical and catalytic properties that are associated with lattice dynamics are likely to be preserved after the treatment.

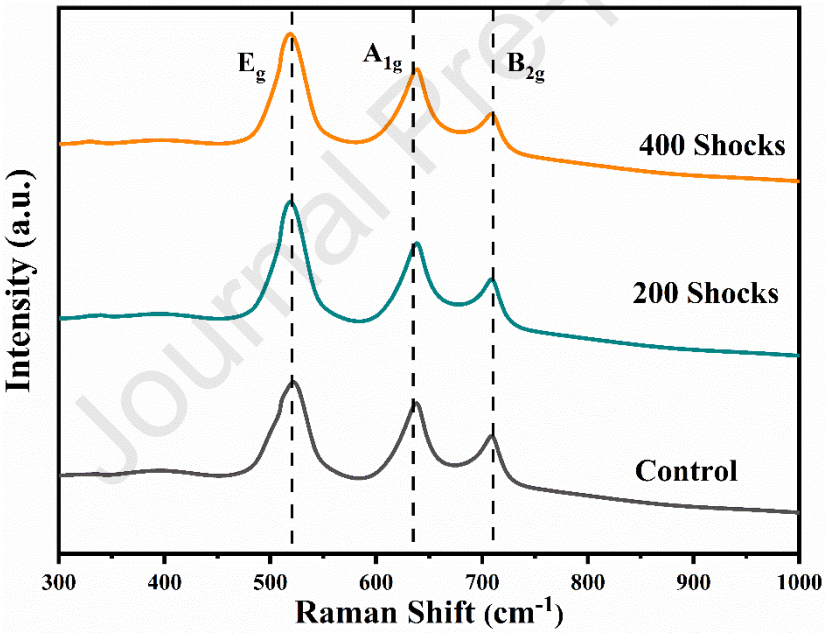

Figure 8: Raman spectra of the control, 200, and 400 shocked RuO_2.

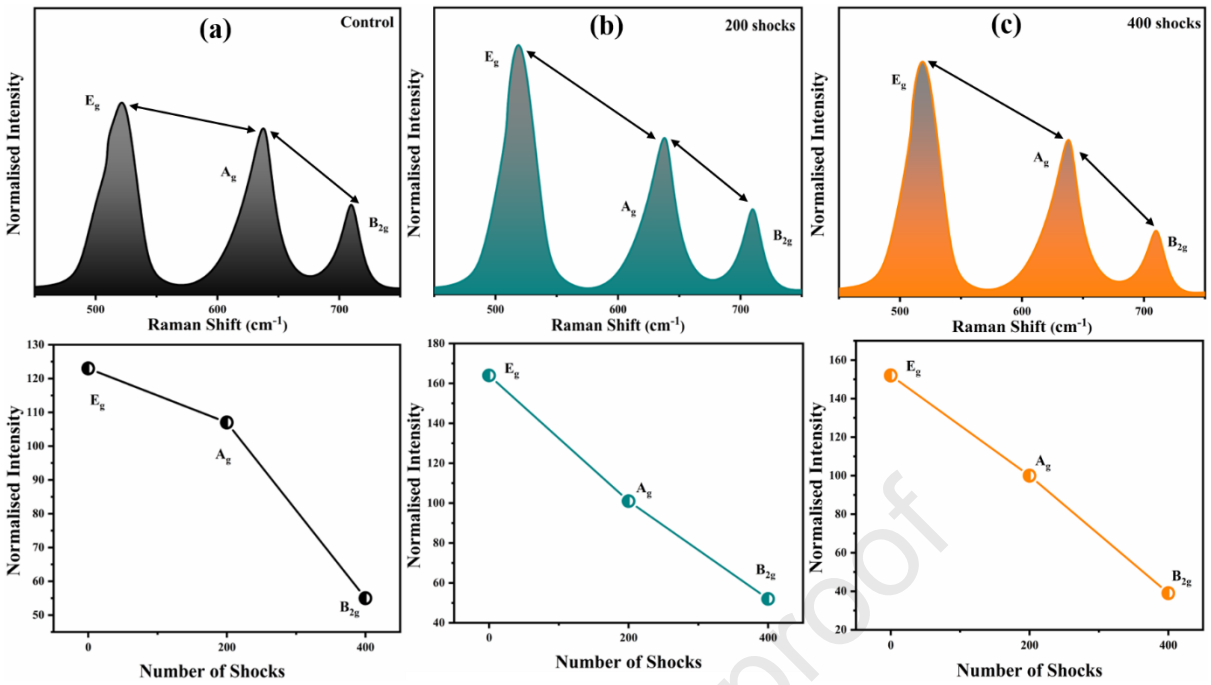

Figure 9: Zoomed-in Raman spectral bands of the **(a)** control, **(b)** 200, and **(c)** 400 shocked RuO_2.

3.6 Optical stability analysis

When contemplating the use of optical characteristics for real-time applications in harsh environments, it is essential to ensure certain qualities, such as stability in optical transmittance. Over a wavelength range that extends from 500 to 2500 nm, the optical transmission of RuO_2 was measured. Fig. 10(a) shows the difference between the optical transmittance spectra of the control and shocked samples. A modest change in reflectance percentage was observed following shock pulse application. The reflectance percentages were 20.5% and 20.9% for the control and 200-shock RuO_2 samples, respectively, increasing to 24.9% for the 400-shock RuO_2, representing a noticeable rise from the previous values. In addition, the Tauc plot was used to compute the indirect optical transition energy. Fig. 10 (b-d) shows the estimated optical transition energy patterns of the control and shocked RuO_2 samples. Following exposure to the

shock waves, the Tauc plot revealed no significant modifications [19]. According to the Tauc plot, the calculated optical transition energy values are 3.6 eV for the control, 200, and 400 shocked samples. The relatively low reflectance in the near infrared makes this material a candidate for the coating of radiative heat flux sensors for spacecraft back shells focused on carbon dioxide measurements [37,38].

$$\alpha = \frac{c(h\gamma - E_g^{bulk})^2}{h\gamma} \quad (1)$$

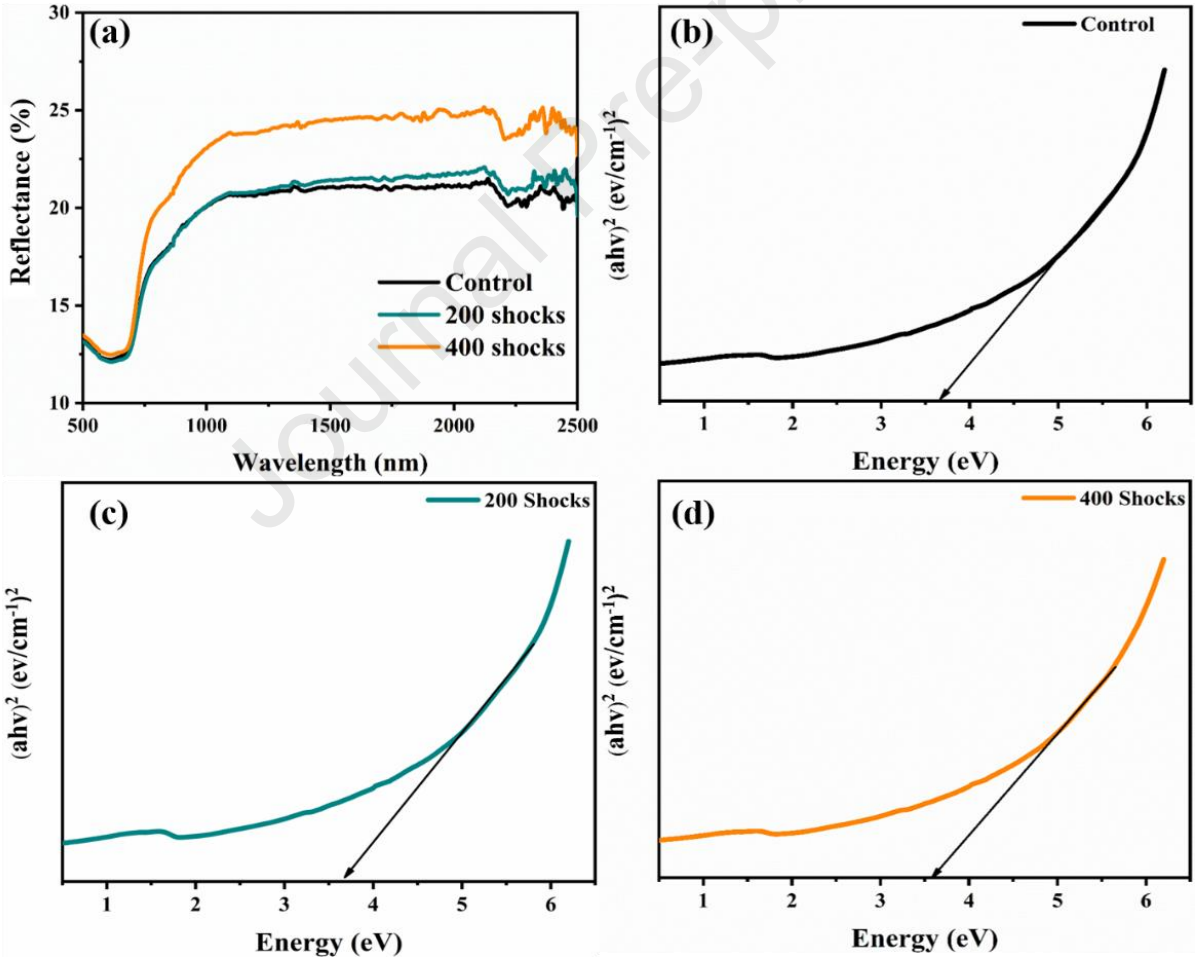

Figure 10: UV DRS plot of the **(a)** control and shocked RuO_2 and Tauc plot of the **(b)** control, **(c)** 200 shocks, **(d)** 400 shocks.

3.7 Calculated optical properties of the RuO_2

The optical properties of the RuO_2, such as its absorption coefficient, dielectric function, energy loss, optical conductivity, reflectivity, and refractive index, were calculated and shown in the Fig. 11-13. The absorption coefficient α(ω) spectrum demonstrates a substantial absorption in the lower photon energy band, which indicates that the material is able to interact with incident photons in an effective manner. It is contained within the ultraviolet spectrum and has a wavelength of 145.88 nm. A straight electronic transition between bands is taking place here. The material's potential for use in optoelectronic and photovoltaic applications is strengthened by the high absorption coefficient values that were observed in the ultraviolet range. Additionally, the dielectric function, which is characterised by its real (ε_1) and imaginary (ε_2) components, offers additional electronic response properties. A peak corresponding to the energy at which interband transitions occur can be observed in the ε_2 spectra. This peak value is in close alignment with the absorption maxima. At low energies, the ε_1 curve exhibits a significant positive value, which indicates that the polarizability is enhanced and that the photon screening process is effective. 826.66 nm is the wavelength of the dielectric function, which is located in the near-infrared part of the electromagnetic spectrum. The results confirmed both a high polarizability and a robust optical activity. It can be utilised in photonic devices and ultraviolet detectors.

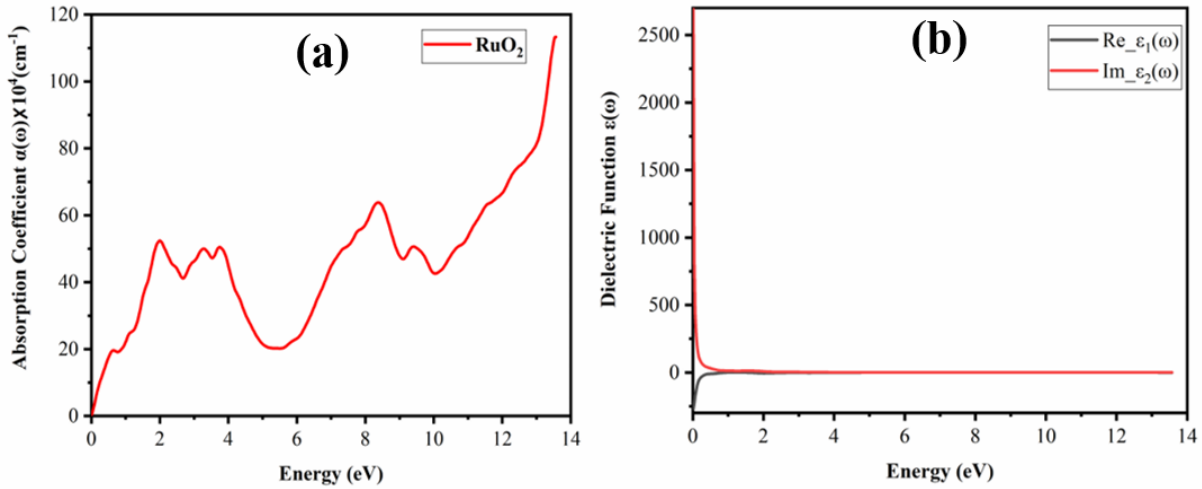

Figure 11: Calculated **(a)** absorption coefficient and **(b)** dielectric function of RuO_2.

A distinct and well-defined peak can be seen in the energy loss spectrum at approximately 4.8 eV. This peak is indicative of the bulk plasmon resonance, which is the point at which valence electrons vibrate collectively. These peak draws attention to the energy at which electrons that are moving at high speed absorb the greatest amount of energy as they move through the material. Eloss has a wavelength of 258.33 nm, which places it in the ultraviolet (UV) zone. When the photon energy is increased beyond this point, the intensity of the loss steadily decreases, which indicates that there are fewer collective excitations associated with higher energies. At around 1.9 eV, the optical conductivity curve experiences a dramatic increase, which corresponds to the absorption edge of the material. The visible light spectrum includes a wavelength of 688.88 nm, which is the wavelength of optical conductivity. Transitions between high-density electronic states in the valence and conduction bands are linked to these characteristics, which are associated with interband transitions. Overall, the spectra indicate that the material exhibits both strong low-energy optical activity and a distinct plasmonic response, consistent with the behaviour of related compounds.

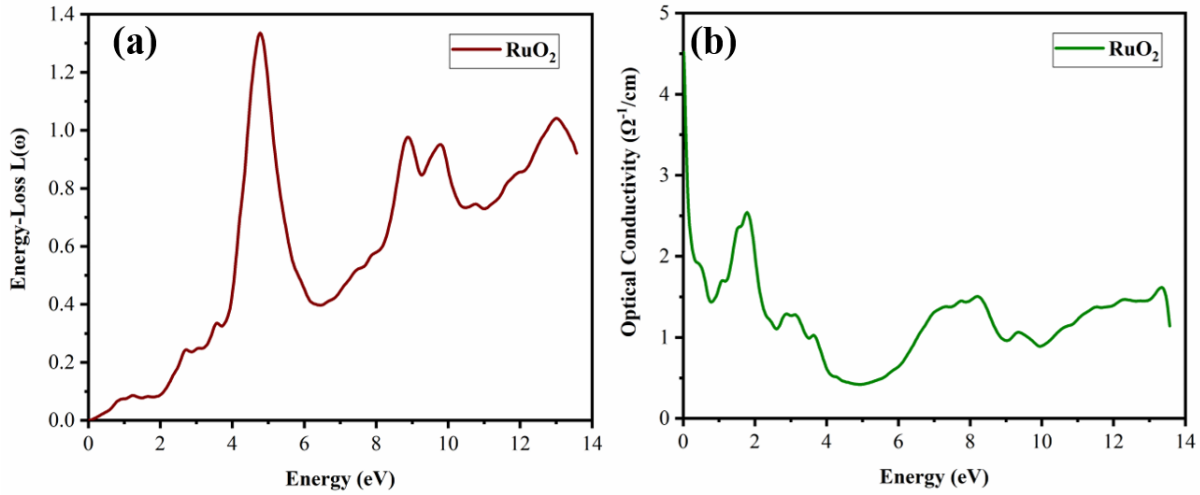

Figure 12: Calculated **(a)** energy loss and **(b)** optical conductivity of RuO_2.

The reflectivity R(ω) begins at a reasonably high value of roughly 0.6 in the low-energy region. This number represents the reflection of light that has been incident upon the substance of interest. Electronic transitions between bands are the cause of the minute oscillations that take place between 1 and 5 eV. Plasmon damping or absorption effects are the agents that are accountable for the decrease in reflection that takes place in the range of 6-10 eV. As a consequence of this process, the reflectivity steadily decreases as the energy of the photon increases. Reflectivity is completely contained inside the visible light spectrum due to its wavelength of 620 nm, which positions it precisely within the spectrum. When the energy of the photon is low, the refractive index n(ω) begins to become quite high, which indicates that the material has a powerful interaction. As the photon energy increases, however, the index decreases by a few electron volts and stays virtually the same throughout the process. The n(ω) reaches approximately 2.3 eV at a wavelength of 826.66 nm, placing it within the near-infrared (NIR) region.

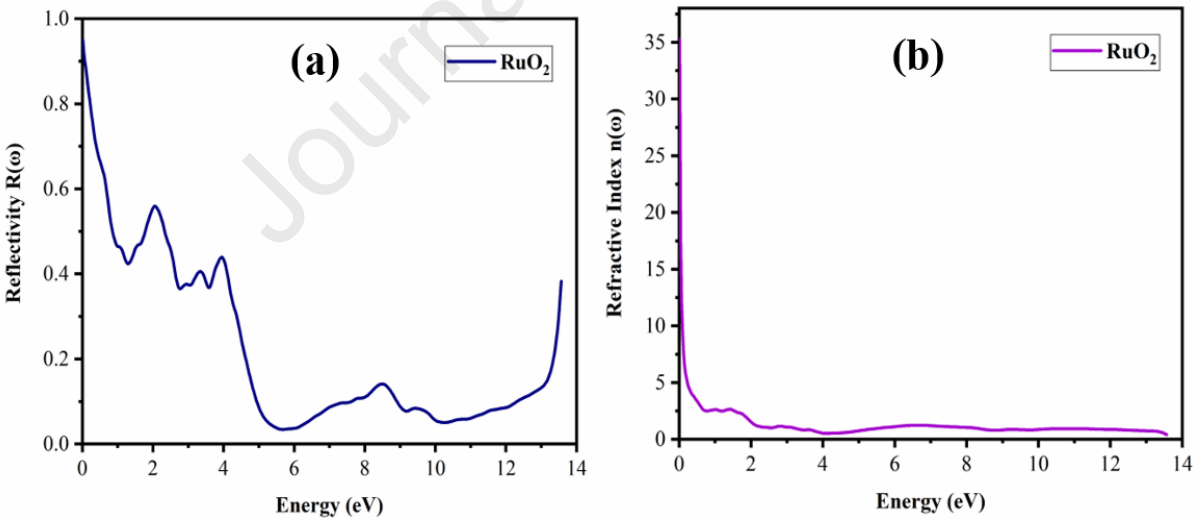

Figure 13: Calculated **(a)** Reflectivity and **(b)** Refractive Index of RuO_2.

3.8. XPS analysis

X-ray photoelectron spectroscopy (XPS) was used to investigate the surface chemical states of RuO_2 samples subjected to dynamic shock treatments.

To evaluate the susceptibility of the ruthenium and oxygen chemical environments to shock conditions, high-resolution spectra for the Ru 3p, Ru 3d, and O 1s regions were analysed. A dominant peak at 462.9 eV is observed in the high-resolution Ru 3p spectra of the control, 200-shock, and 400-shock RuO_2 samples; this peak is typical of the Ru $3p_{1/2}$ and Ru $3p_{3/2}$ species in rutile-type RuO_2 (refer to Fig. 14(a)). Regardless of the shock treatment, the consistent peak position in all samples indicates that the Ru oxidation state was preserved [39]. A weak shoulder at 464.7 eV indicates a small degree of surface reduction or oxygen vacancy formation, corresponding to the presence of Ru $3p_{3/2}$ species. For each sample, the relative abundance of reduced Ru species was measured by calculating the integrated area ratio of Ru $3p_{1/2}$ and Ru $3p_{3/2}$ [40]. Ratios like these did not change much between the control, 200-shock, and 400-shock samples, further showing that shock exposure does not significantly change the distribution of ruthenium's oxidation state. Despite being subjected to several shock treatments that cause tremendous mechanical stress, the predominant $3p_{3/2}$ state remained essentially unchanged, and a uniform trace presence of $3p_{1/2}$ was seen across all samples, highlighting the robust chemical stability of RuO_2. High-resolution XPS spectra of the Ru 3d region are shown in the middle panel of Fig. 14(b). These spectra are for both the control and shock-treated RuO_2 nanoparticles, which were subjected to 200 and 400 shocks, respectively. The Ru 3d spectrum is deconvoluted into four major peaks that correspond to Ru $3d_{5/2}$, Ru $3d_{3/2}$, and C 1s [41]. These peaks are commonly detected around 280.0 - 284.0 eV, which is consistent with previous reports. The peak Ru 3d typically aligns with the peak for Adventitious Carbon (C 1s). Overall, the Ru 3d XPS results confirm that RuO_2 retains its structural integrity and oxidation state even after repeated shock wave exposure, highlighting its remarkable chemical stability and robustness. A prominent peak centred at approximately 530.2 eV is visible in the O 1s spectra of all three samples, which is thought to be caused by the lattice oxygen (O^{3-}) in RuO_2, shown in Fig. 14(c). There is a little shoulder at around

531.5% eV that could be caused by oxygen atoms coupled with defects or adsorbed surface hydroxyl species. The oxygen atmosphere in RuO_2 appears chemically robust and resistant to shock-induced stress, as the relative intensity and positions of these peaks showed minimal changes under the control, 200-shock, and 400-shock conditions. XPS analysis of the Ru 3p and O 1s regions revealed no significant changes in oxidation states or chemical shifts in RuO_2 samples subjected to shock treatments up to 400 shocks. The remarkable chemical and structural stability of the RuO_2 under dynamic shock conditions is confirmed by the survival of characteristic lattice O^3 and Ru^{4+} peaks in all spectra. Applications such as catalysis and aerospace systems, which are exposed to mechanical extremes, could benefit from this material's stability.

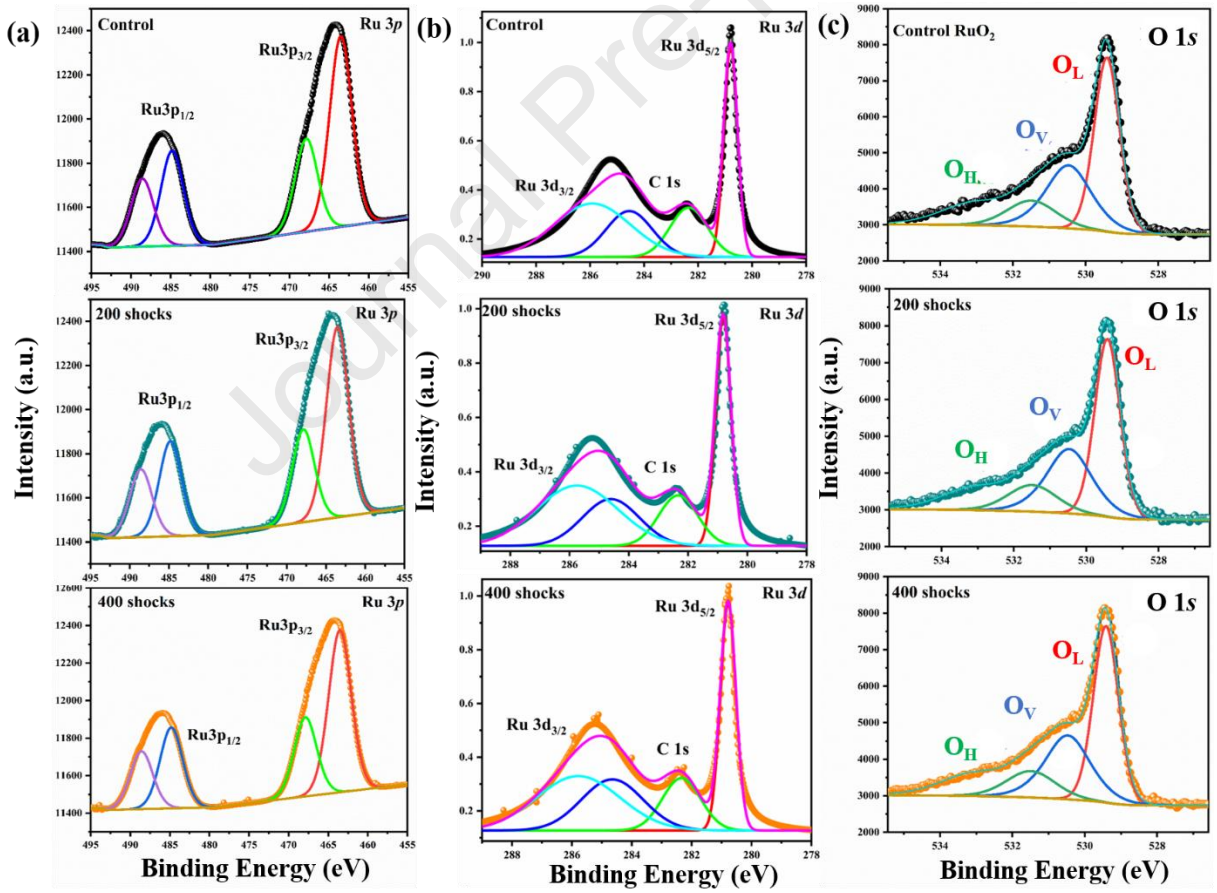

Figure 14: XPS deconvolution **(a)** Ru 3p, **(b)** Ru 3d, and **(c)** O 1s for the control, 200, and 400 shock-treated RuO_2.

3.9 Band structure and density of states of RuO_2

The electronic structure of RuO_2 was investigated by band structure analysis along with the total and partial density of states (TDOS and PDOS) calculations, which are shown in Fig. 15. The results clearly indicate that RuO_2 exhibits a metallic behaviour, as the valence and conduction bands overlap around the Fermi level. This metallic character arises primarily from the hybridisation between the Ru 4d states and O 2p states, with the Ru 4d orbitals contributing significantly near the Fermi level. The strong Ru O covalent bonding is evident from this hybridisation. Both the TDOS and PDOS consistently confirm the metallic nature of RuO_2. The DOS analysis further reveals that the Ru 4d orbitals dominate at the Fermi level, while the O 2p orbitals mainly contribute at lower energies within the valence band. At higher energies above the Fermi level, unoccupied Ru 4d states are widely dispersed, reinforcing the metallic character. The presence of a high density of states around the Fermi level also suggests enhanced electrical conductivity, in good agreement with available experimental observations.

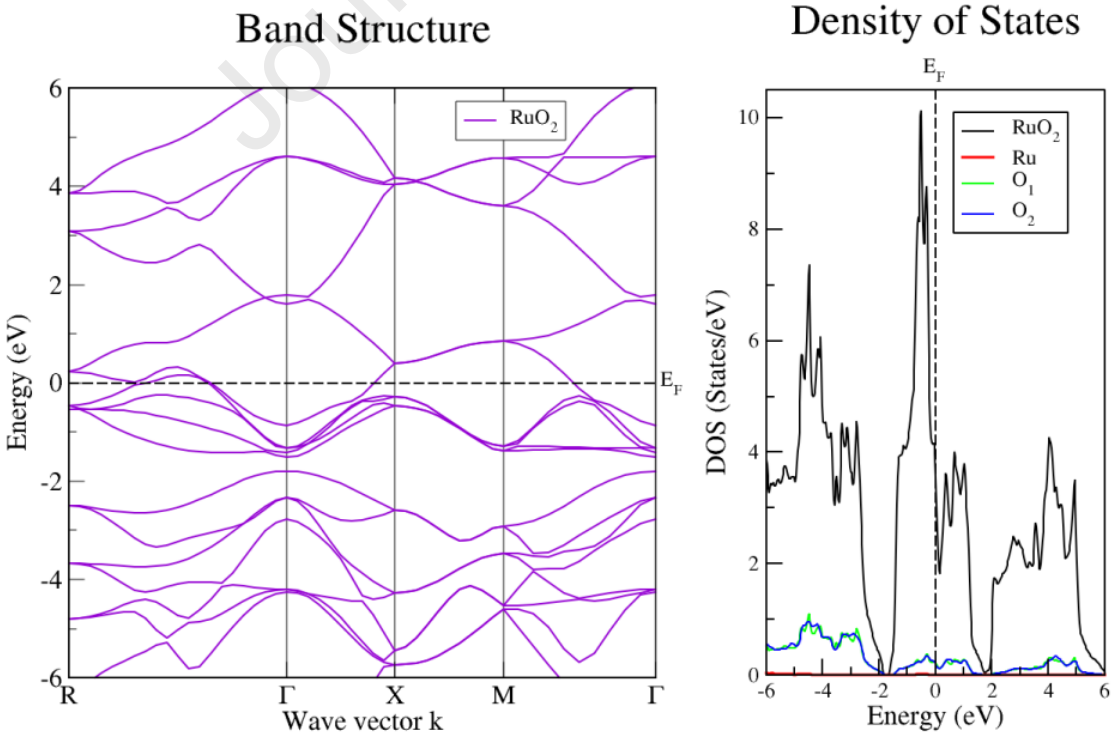

Figure 15: The band structure and total and partial density of states of RuO_2.

3.10. Photocatalytic analysis

Methylene blue dye is a major contributor to water pollution and is widely used for dying in many different industries [42,43]. To test the photo-assisted degradation % of the control and shocked RuO_2, we exposed them to sunlight. Fig. 16 (a-c) shows the control and the varying photo-assisted degradation of the materials after 200 and 400 shock treatments. The absorbance at 664 nm gradually decreased over time, indicating that the dye was actively degrading under light exposure. It is important to note that the photo-assisted degradation stability of RuO_2 remained unchanged in both the control and shock-treated samples. This result indicates that the active surface locations and the structural integrity were not affected by the ever-changing environment.

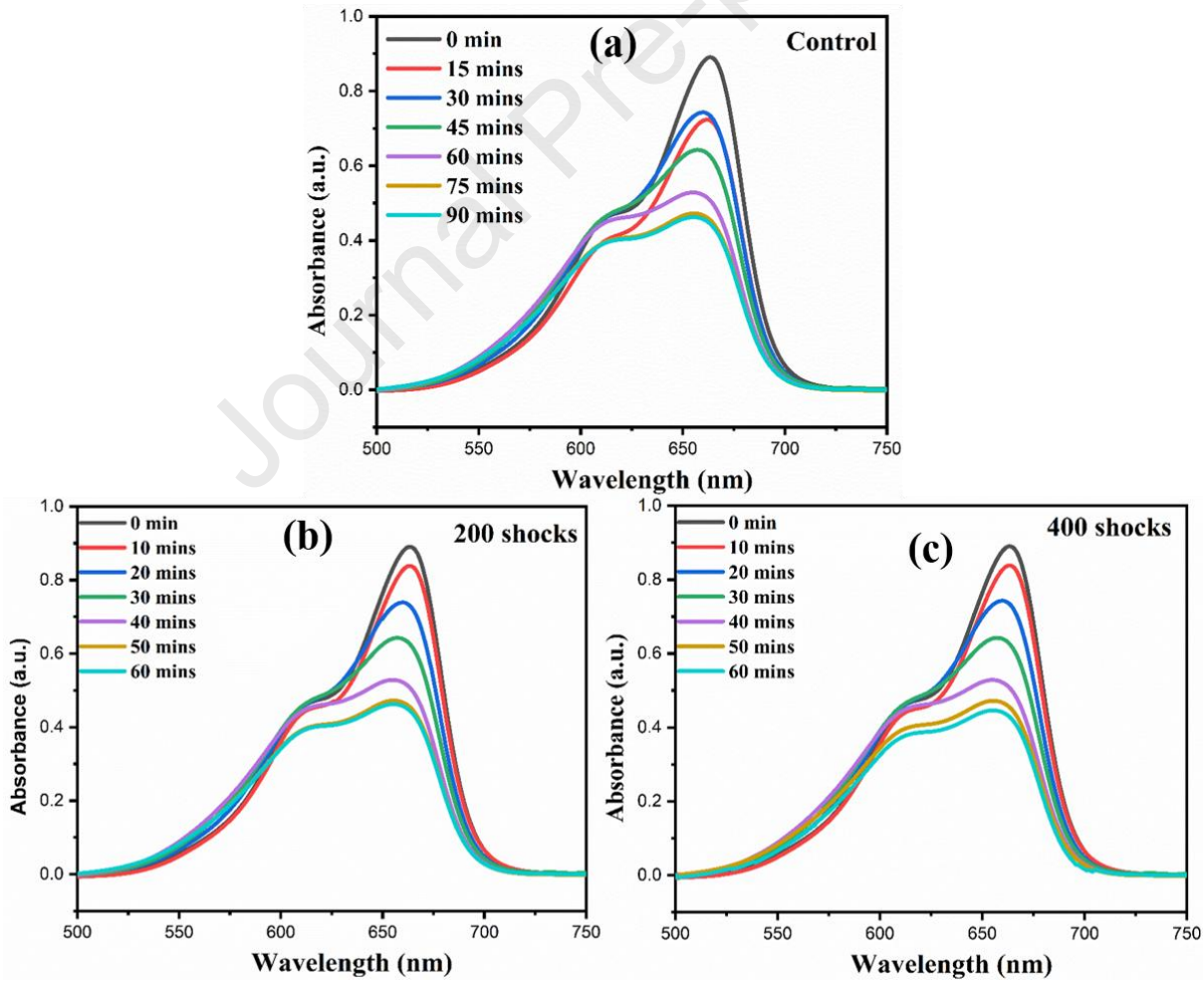

Figure 16: Absorbance spectra of the MB dye for the **(a)** control RuO_2, **(b)** 200 shocks, **(c)** 400 shocks.

This result is further supported by the observation that the degradation efficiency remained consistently above 48% for all samples after 60 minutes of exposure, as shown in Fig. 17(c,d). The efficiency of RuO_2 was calculated using the formula

$$Degradation\ efficiency\ (\eta)\% = \frac{(A_0 - A_t)}{A_0} \times 100\,. \qquad \textbf{(2)}$$

A pseudo-first-order kinetic model was used to match the experimental data to have a better understanding of the degradation process kinetics as follows:

$$ln\frac{C_0}{C_t} = kt. \qquad \textbf{(3)}$$

In this equation, the quantities C_0 and C_t represent the concentrations of the dye at time zero and time t, respectively, while k represents the apparent rate constant. The linear fitting of the kinetic plots for all three samples, control, 200-shock, and 400-shock treated RuO_2 samples, revealed good correlation coefficients (R2 > 0.98), demonstrating that pseudo first-order kinetics were adhered to, as seen in Fig. 17. This result indicates that the shock wave treatment did not significant impact the photo-assisted degradation behaviour of RuO_2; the rate constants that were determined for the three samples turned out unaltered. The rate constants that were determined were as follows: 0.0081 min^{-1} for the control, 0.0081 min^{-1} for the 200-shock sample, and 0.0084 min^{-1} for the 400-shock sample. These findings show that RuO_2's surface reactivity remains largely unaffected within the bounds of dye-based studies, even when subjected to dynamic mechanical stress, as evidenced by the fact that the values of k did not vary much as the shock intensity increased. These results further support the structural and functional stability of RuO_2 nanoparticles under harsh conditions, in agreement with the XRD, SEM, and UV analysis findings. The reduction in absorbance does not directly reflect intrinsic charge-carrier formation in the photocatalyst, but rather represents general photo-assisted dye degradation due to the fact that methylene blue can act as a photosensitiser when exposed to light. So, without limiting the

degradation to band-edge-driven catalytic pathways, the current data are analysed in a comparable way under the same experimental conditions.

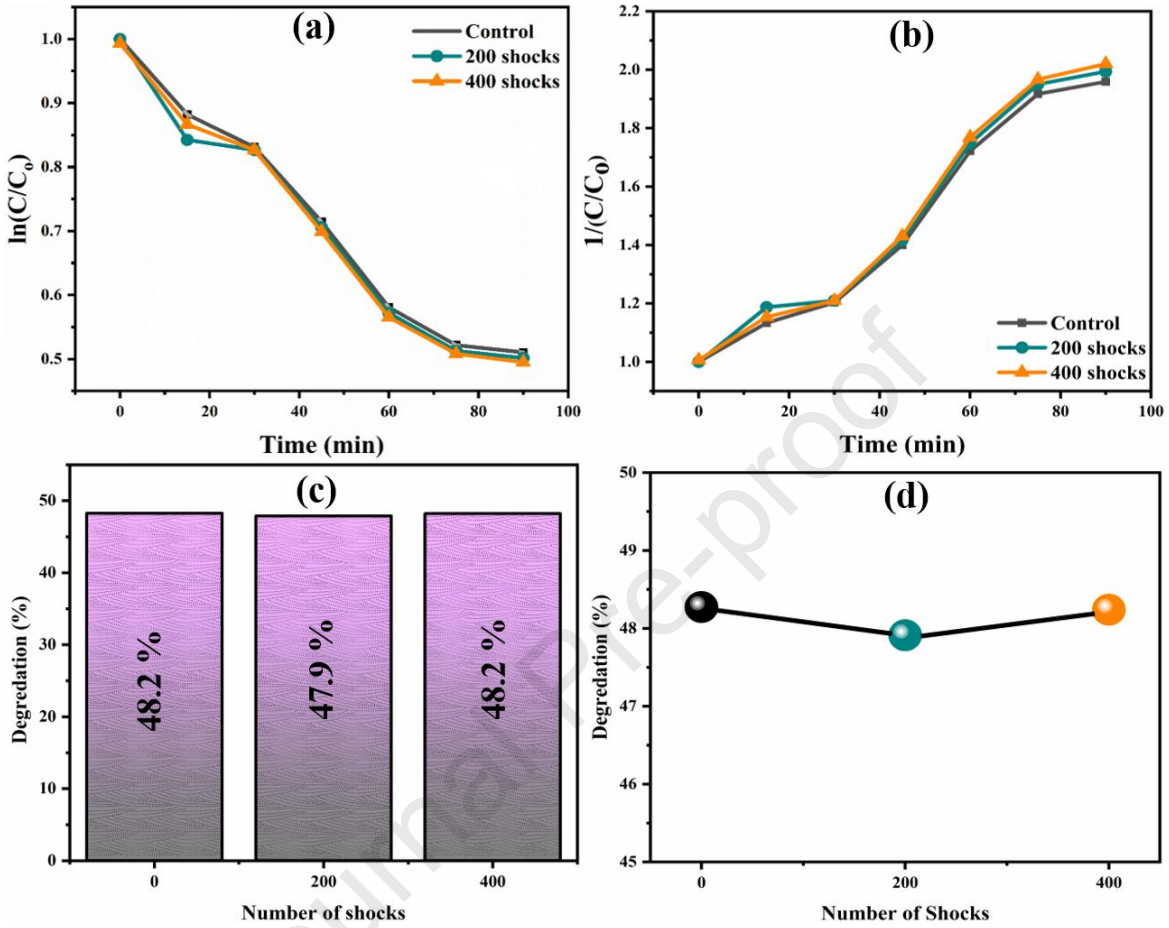

Figure 17: Catalytic performance **(a&b)** pseudo-first-order kinetics, **(c)** efficiency histogram, **(d)** efficiency comparison for the control and shocked RuO_2.

4. Conclusions

This study presents a comprehensive evaluation of the structural, optical, morphological, and catalytic stability of RuO_2 nanoparticles using experimental and theoretical analyses with a semi-automatic shock tube. Despite subjecting the material to 400 shock pulses, the XRD results show no signs of a phase transition under shocked conditions. Results from the DFT calculations reveal that RuO_2 crystallises as a stable tetragonal rutile, with optimised lattice constants that

closely match experimental data. Based on the SEM findings, it was confirmed that there is a slight reduction in grain size in the 400-shock-wave-loaded RuO_2 NPs. The FTIR results suggest that the RuO_2 NPs are stable except for a slight modification in the OH stretching in the 400-shock-treated sample. The optical properties were stable throughout the shock wave experiment, with an estimated optical transition energy value of 3.6 eV. The XPS results revealed that RuO_2 remains chemically stable after 200 and 400 shock treatments, with no significant changes in Ru or O oxidation states. DOS and band structure analyses confirmed the metallic nature of RuO_2, resulting from the significant hybridisation between the Ru 4d and O 2p orbitals. Regardless of the number of shocks administered, the photo-assisted degradation breakdown of methylene blue in sunlight followed pseudo-first-order kinetics. Shock-induced mechanical stress appears to have little effect on the photo-assisted degradation activity of RuO_2, as the apparent rate constants remained largely unchanged. The material exhibited exceptional stability under stress conditions, indicating its potential for use in robust photo-assisted degradation systems where durability is crucial. Despite the fact that the photo-assisted degradation behaviour of RuO_2 was determined to be ~ 48 %, the material exhibited exceptional stability. Taking everything into account, the findings strongly suggest that RuO_2 possesses an exceptional blend of electrical conductivity, optical activity, and remarkable mechanical stability. The combined insights from first-principles calculations and shock-wave experiments demonstrate that RuO_2 possesses exceptional structural resilience and stability, rendering it a promising candidate for next-generation hypersonic and aerospace materials.

Data Availability

All the data used in the manuscript are within the manuscript

Conflicts of Interest

The authors declare that they have no conflicts of interest

Consent for publication

Not applicable

Ethics approval and consent to participate

Not available

Acknowledgements

The authors would like to thank the National Research Foundation of Korea (NRF) grant, funded by the Korean government (MIST) (RS-2025-14383145).

Credit Author Statement

Surendhar Sakthivel: Methodology, Investigation, Writing – Original Draft.
Sivaprakash Paramasivam: Formal analysis, software.
Martin Britto Dhas Sathyadhas Amalapushpam: Supervision, Formal analysis, Review & Editing.
Aravindan Vivekanandan: Software, Validation.
Jithesh Ramakrishnan Kannan: Software.
Tobias Hermann: Review & Editing, Formal analysis.
Ikhyun Kim: Supervision, Funding acquisition, Review & Editing.

References

[1] S. Aswathappa, L. Dai, S.J. Dhas Sathiyadhas, R.S. Kumar, Artificial acoustic shock wave processing on α- Quartz single crystal-towards the formation of disordered state – A Raman spectroscopic approach, Ceram. Int. 51 (2025) 15973–15982. https://doi.org/10.1016/j.ceramint.2025.01.433.
[2] S.A. Kumar, S.S.R. Inbanathan, R.B. Vignesh, D.R. Rosaline, B.R. Kamalam, A. Umar, A.A. Ibrahim, S. Akbar, S.A.M.B. Dhas, S. Baskoutas, Shock wave pulsed strategy on green synthesized nickel oxide nanoparticles: Structural, morphological, and electrochemical performance,

Ceram. Int. 51 (2025) 4509–4520. https://doi.org/10.1016/j.ceramint.2024.11.426.
[3] A. Sivakumar, S. Sahaya Jude Dhas, S.A. Martin Britto Dhas, Impact of shock waves on vibrational and structural properties of glycine phosphite, Solid State Sci. 110 (2020) 106452. https://doi.org/10.1016/j.solidstatesciences.2020.106452.
[4] S. Surendhar, P. Sivaprakash, J. Jerries Infanta, R. Jagadeesh, S.A. Martin Britto Dhas, I. Kim, S. Arumugam, Enhancing the efficiency of gas sensing on perovskite BaTiO3 nanoparticles using dynamic shock wave flow environment, Ceram. Int. 50 (2024) 23710–23720. https://doi.org/10.1016/j.ceramint.2024.04.094.
[5] Z. Su, W.L. Shaw, Y.-R. Miao, S. You, D.D. Dlott, K.S. Suslick, Shock Wave Chemistry in a Metal-Organic Framework, J. Am. Chem. Soc. 139 (2017) 4619–4622. https://doi.org/10.1021/jacs.6b12956.
[6] A Siva kumar, P. Eniya, S. Sahaya Jude Dhas, Abdulrahman I. Almansour, Raju Suresh Kumar, Natarajan Arumugam, J. Kalyana Sundar, Shubhadip Chakraborty, S.A. Martin Britto Dhas, Switchable phase transition of crystalline to amorphous state of potassium nitrate single crystal, Surf. Interfaces 35 (2022) 102422. https://doi.org/10.1016/j.surfin.2022.102422.
[7] D. Errandonea, D. Santamaria-Perez, D. Martínez-García, O. Gomis, R. Shukla, S. Achary, A. Tyagi, C. Popescu, Pressure Impact on the Stability and Distortion of the Crystal Structure of CeScO 3, Inorg. Chem. 56 (2017). https://doi.org/10.1021/acs.inorgchem.7b01042.
[8] S. Aswathappa, L. Dai, S.J. Dhas Sathiyadhas, M.B. Dhas Sathiyadhas Amalapushpam, M. Vijayan, R. Suresh Kumar, A.I. Almansour, Acoustic shock wave recovery experiments on cubic zinc sulfide nanoparticles for electrical and magnetic switches applications, Ceram. Int. 50 (2024) 7418–7430. https://doi.org/10.1016/j.ceramint.2023.12.028.
[9] A. Sivakumar, C. Victor, M.M. Nayak, S.A.M.B. Dhas, Structural, optical, and morphological stability of ZnO nano rods under shock wave loading conditions, Mater. Res. Express 6 (2019) 045031. https://doi.org/10.1088/2053-1591/aafae6.
[10] A. Rita, A. Sivakumar, S.S.J. Dhas, S.A.M.B. Dhas, Structural, optical and magnetic properties of silver oxide (AgO) nanoparticles at shocked conditions, J. Nanostructure Chem. 10 (2020) 309–316. https://doi.org/10.1007/s40097-020-00351-z.
[11] T. Abe, S. Inoue, K. Watanabe, XRD and electrochemical measurements of RuO2 powder treated by using a mechanical grinding method, J. Alloys Compd. 358 (2003) 177–181. https://doi.org/10.1016/S0925-8388(03)00045-8.
[12] T. Tang, K. Chen, X. Wang, Y. Liu, Z. Zheng, X. Shen, L. Li, X. Zheng, S. Xiao, Y. Chen, X. Du, Investigation on the temperature-dependent

mechanism shift of CO oxidation over RuO2/TiO2 catalysts, Surf. Interfaces 70 (2025) 106891. https://doi.org/10.1016/j.surfin.2025.106891.
[13] S. Chen, H. Huang, P. Jiang, K. Yang, J. Diao, S. Gong, S. Liu, M. Huang, H. Wang, Q. Chen, Mn-Doped RuO $_2$ Nanocrystals as Highly Active Electrocatalysts for Enhanced Oxygen Evolution in Acidic Media, ACS Catal. 10 (2020) 1152–1160. https://doi.org/10.1021/acscatal.9b04922.
[14] W.T. Lim, K.R. Cho, C.H. Lee, Structural and electrical properties of rf-sputtered RuO2 films having different conditions of preparation, Thin Solid Films 348 (1999) 56–62. https://doi.org/10.1016/S0040-6090(99)00015-2.
[15] Md.T. Uddin, O. Babot, L. Thomas, C. Olivier, M. Redaelli, M. D'Arienzo, F. Morazzoni, W. Jaegermann, N. Rockstroh, H. Junge, T. Toupance, New Insights into the Photocatalytic Properties of RuO2/TiO2 Mesoporous Heterostructures for Hydrogen Production and Organic Pollutant Photodecomposition, J. Phys. Chem. C 119 (2015) 7006–7015. https://doi.org/10.1021/jp512769u.
[16] A.M. Huerta-Flores, F. Ruiz-Zepeda, C. Eyovge, J.P. Winczewski, M. Vandichel, M. Gaberšček, N.D. Boscher, H.J.G.E. Gardeniers, L.M. Torres-Martínez, A. Susarrey-Arce, Enhanced Photocatalytic Hydrogen Evolution from Water Splitting on Ta2O5/SrZrO3 Heterostructures Decorated with CuxO/RuO2 Cocatalysts, ACS Appl. Mater. Interfaces 14 (2022) 31767–31781. https://doi.org/10.1021/acsami.2c02520.
[17] D.A. Reddy, R. Ma, T.K. Kim, Efficient photocatalytic degradation of methylene blue by heterostructured ZnO–RGO/RuO2 nanocomposite under the simulated sunlight irradiation, Ceram. Int. 41 (2015) 6999–7009. https://doi.org/10.1016/j.ceramint.2015.01.155.
[18] S. Sakthivel, S. Paramasivam, P. Velusamy, S.A.M. Britto Dhas, A. Sonachalam, I. Kim, Tuning photocatalytic activity of Ce-doped BaTiO3 nanoparticles by encountering acoustic shock wave flow exposure, Ceram. Int. 51 (2025) 13003–13017. https://doi.org/10.1016/j.ceramint.2025.01.147.
[19] N.R. Barveen, B. Parasuraman, P.-Y. Wang, C.-W. Zeng, Y.-W. Cheng, P. Thangavelu, Facile construction of ZnWO4/g-C3N4 heterojunction for the improved photocatalytic degradation of MB, RhB and mixed dyes, Surf. Interfaces 53 (2024) 105039. https://doi.org/10.1016/j.surfin.2024.105039.
[20] A. Murugan, A. Fatehmulla, S. Priya, S.S. Han, S. Babu, C. Rohit, S. Bharathkumar, Optimizing the photocatalytic properties Er-doped bismuth ferrite for the degradation of mixed dyes under sunlight irradiation, Surf. Interfaces 54 (2024) 105239. https://doi.org/10.1016/j.surfin.2024.105239.
[21] S. Surendhar, X. T. Peter, P. Sivaprakash, P. Malar, S.A.M.B. Dhas, S. Arumugam, I. Kim, Shock wave-driven phase transition of iron sulphide for enhanced photocatalytic application: a combined experimental and DFT approach, RSC Adv. 15 (2025) 22432–22448. https://doi.org/10.1039/D5RA03559G.

[22] S. Surendhar, I. Kim, P. Sivaprakash, S.H. Cho, Sustainability of Fluorine-Tin Co-Doped Indium Oxide (F,Sn:In2O3) Nanocrystals at Various Shock Speeds Under Dynamic Shocked Conditions, Natl. Acad. Sci. Lett. (2025). https://doi.org/10.1007/s40009-025-01724-0.
[23] K.P.J. Reddy, N. Sharath, Manually operated piston-driven shock tube, Curr. Sci. 104 (2013).
[24] S. Sakthivel, S. Paramasivam, P. Velusamy, J.A.D. Jerries Infanta, V. Ragavendran, J. Mayandi, S. Arumugam, I. Kim, Experimental investigation of structural, morphological, and optical characteristics of $SrTiO_3$ nanoparticles using a shock tube for photocatalytic applications, Z. Für Phys. Chem. 0 (2024). https://doi.org/10.1515/zpch-2023-0486.
[25] J. Schaefer, E.W.K. Chang, T. Hermann, S. Loehle, Experimental Investigation of a Small-scale Arc-jet for Earth Entry Simulation, in: AIAA SCITECH 2024 Forum, American Institute of Aeronautics and Astronautics, 2024. https://doi.org/10.2514/6.2024-2571.
[26] N. Laihnuna, B. Djamel, V. Aravindan, E.-A. Haidar, Z. Pachuau, J. Lalbiakkima, T.H. Lalrinmawii, Malsawmtluanga, G.C. Lalremruata, L. Sailo, Multifaceted analysis of K2InAgX6 (X = F, Cl, Br, I) for photovoltaic and thermoelectric applications, J. Phys. Chem. Solids 195 (2024) 112291. https://doi.org/10.1016/j.jpcs.2024.112291.
[27] V. Aravindan, V. Vijayanarayanan, B. Karuppasamy, K. Sakthipandi, M. Mahendran, First-principles study on rare earth-based equiatomic quaternary Heusler alloys YbCoCrSb and YbCoTiSn: New candidates for spintronics, Mater. Today Commun. 39 (2024) 108599. https://doi.org/10.1016/j.mtcomm.2024.108599.
[28] M. Nandha Kumar, V. Aravindan, N. Laihnuna, M. Mahendran, Rare earth-based LaCoCrZ (Z=In, Sn, Sb) equiatomic quaternary Heusler alloys: Materials for high-temperature thermoelectrics, J. Rare Earths (2025). https://doi.org/10.1016/j.jre.2025.06.021.
[29] S. Neupane, G. Kaganas, R. Valenzuela, L. Kumari, X. Wang, W. Li, Synthesis and Characterization of Ruthenium Dioxide Nanostructures, J. Mater. Sci. 46 (2011) 4803–4811. https://doi.org/10.1007/s10853-011-5390-2.
[30] S. Aswathappa, E. Palaniyasan, S.J.D. Sathiyadhas, K.S. Jayaperumal, S. Paramasivam, A. Sonachalam, M.B.D.S. Amalapushpam, Shock wave induced defect engineering on structural and optical properties of pure and dye doped potassium dihydrogen phosphate crystals, Z. Für Krist. - Cryst. Mater. 235 (2020) 193–202. https://doi.org/10.1515/zkri-2020-0017.
[31] S. Daolio, J. Kristóf, C. Piccirillo, C. Pagnra, A.D. Battisti, Investigation of the formation of RuO2-based mixed oxide coatings by secondary ion mass spectrometry, J. Mater. Chem. 6 (1996) 567–571. https://doi.org/10.1039/JM9960600567.

[32] S. Karuppuchamy, J.M. Jeong, Synthesis of Nano-particles of TiO2 by Simple Aqueous Route, J. Oleo Sci. 55 (2006) 263–266. https://doi.org/10.5650/jos.55.263.
[33] M. Angermann, G. Jakopic, C. Prietl, T. Griesser, K. Reichmann, M. Deluca, Highly conductive RuO2 thin films from novel facile aqueous chemical solution deposition, J. Sol-Gel Sci. Technol. 108 (2023) 575–587. https://doi.org/10.1007/s10971-023-06221-8.
[34] S. Aswathappa, L. Dai, S.J.D. Sathiyadhas, R.S. Kumar, Acoustic shock wave-induced superheating-assisted dynamic recrystallization – a case study of D-tartaric acid, Phys. Chem. Chem. Phys. 27 (2024) 308–315. https://doi.org/10.1039/D4CP03750B.
[35] S. Aswathappa, L. Dai, S.J. Dhas Sathiyadhas, R.S. Kumar, A.I. Almansour, C.L. Selvakumar, V.V. Nallagounder, V. Panneerselvam, Acoustic shock-wave induced structural phase transition (ordered-to-disordered) associated dielectric transition (space charge-to-dipolar polarization): A case study of structure–property relationship in lithium sulfate monohydrate single crystal, J. Chem. Phys. 163 (2025) 164705. https://doi.org/10.1063/5.0296849.
[36] S. Aswathappa, L. Dai, S.S.J. Dhas, R.S. Kumar, Artificial Acoustic Shock Wave-Induced Lattice Distortion-Driven Structural Order–Disorder Phase Transition in Natural Polycrystalline Forsterite (α-Mg2SiO4): X-Ray and Raman Spectroscopic Approaches, J. Raman Spectrosc. 56 (2025) 609–622. https://doi.org/10.1002/jrs.6814.
[37] T.K. West, J. Theisinger, A.J. Brune, C.O. Johnston, Backshell Radiative Heating on Human-Scale Mars Entry Vehicles, in: 47th AIAA Thermophys. Conf., American Institute of Aeronautics and Astronautics, 2017. https://doi.org/10.2514/6.2017-4532.
[38] B.A. Cruden, D. Prabhu, R. Martinez, Absolute Radiation Measurement in Venus and Mars Entry Conditions, J. Spacecr. Rockets 49 (2012) 1069–1079. https://doi.org/10.2514/1.A32204.
[39] D.J. Morgan, Resolving ruthenium: XPS studies of common ruthenium materials, Surf. Interface Anal. 47 (2015) 1072–1079. https://doi.org/10.1002/sia.5852.
[40] X. Chen, X. Fu, S. Zhang, M. Wang, M. Yuan, Graphdiyne in-situ thermal reduction enabled ultra-small quasi-core/shell Ru-RuO2 heterostructures for efficient acidic water oxidation, 2D Mater. 8 (2021) 044011. https://doi.org/10.1088/2053-1583/ac26db.
[41] D. Rochefort, P. Dabo, D. Guay, P.M.A. Sherwood, XPS investigations of thermally prepared RuO2 electrodes in reductive conditions, Electrochimica Acta 48 (2003) 4245–4252. https://doi.org/10.1016/S0013-4686(03)00611-X.
[42] A. Negash, S. Mohammed, H.D. Weldekirstos, A.D. Ambaye, M. Gashu, Enhanced photocatalytic degradation of methylene blue dye using eco-

friendly synthesized rGO@ZnO nanocomposites, Sci. Rep. 13 (2023) 22234. https://doi.org/10.1038/s41598-023-48826-7.

[43] Z. Kalaycıoğlu, B. Özuğur Uysal, Ö. Pekcan, F.B. Erim, Efficient Photocatalytic Degradation of Methylene Blue Dye from Aqueous Solution with Cerium Oxide Nanoparticles and Graphene Oxide-Doped Polyacrylamide, ACS Omega 8 (2023) 13004–13015. https://doi.org/10.1021/acsomega.3c00198.

Declaration of competing interest

The authors declare that they have no known competing financial interests or personal relationships that could have appeared to influence the work reported in the manuscript